Separating and quantifying ionospheric responses to proton and electron precipitation over Svalbard

Betty Lanchester,[1] Olli-Pekka Jokiaho,[1,2] Marina Galand,[3] Nickolay Ivchenko,[4] Dirk Lummerzheim,[5] Jeff Baumgardner,[2] and Supriya Chakrabarti[2]

Received 14 January 2011; revised 28 June 2011; accepted 6 July 2011; published 27 September 2011.

[1] On 16 December 2001, a variable and structured aurora associated with a period of high solar wind velocity and low solar wind density was recorded through optical, radar, and particle measurements from the ground and space. A comprehensive analysis of this data set is carried out using a coupled auroral electron deposition and ion chemistry model. The observations include H β, N_2^+ 1N (0, 2), and O^+ ^4P-^4D optical and electron density radar measurements from the ground, particle data from NOAA 16 and DMSP F14 satellites, and Doppler-shifted H Lyman α images from the IMAGE satellite. Modulations in the energy flux of both protons and electrons are seen in the NOAA 16 data as well as in the optical signatures measured on ground and from above. At the time of closest approach of NOAA 16, the observed emissions and electron density at the peak of an enhancement are well reproduced when precipitating protons and electrons with total fluxes of 0.23 and 3.0 mW m^{-2}, respectively, and mean energies of 2.50 and 0.25 keV, respectively, are used as input for the model. These values are consistent with those measured by the NOAA satellite. The resulting modeled emissions agree well with the ground measurements of enhanced emissions. The correlation between the emissions from N_2^+ and O^+ suggests that they are primarily due to electron precipitation. This result is confirmed by the agreement between the measured and modeled emissions and by the values of extinction obtained for all three emissions. The modulations to the *E* region ionization can be explained by proton precipitation alone, while soft electrons are responsible for the changes to the ionization at higher altitudes.

Citation: Lanchester, B., O.-P. Jokiaho, M. Galand, N. Ivchenko, D. Lummerzheim, J. Baumgardner, and S. Chakrabarti (2011), Separating and quantifying ionospheric responses to proton and electron precipitation over Svalbard, *J. Geophys. Res.*, *116*, A09322, doi:10.1029/2011JA016474.

1. Introduction

[2] At Earth, auroral emissions are induced by both energetic electrons and protons precipitating from terrestrial magnetospheric regions or entering from the interplanetary regions through the cusp. Doppler-shifted hydrogen emissions, such as Balmer H α and H β and Lyman α, are the result of charge-exchange reactions in the incident proton beam producing energetic H atoms [*Eather*, 1967; *Rees*, 1982; *Frey et al.*, 2003]. These H atoms can become excited when they are produced through capture or when they undergo direct excitation reactions. Unlike electrons, the incident proton beam is affected by lateral spreading due to the presence of neutral H atoms [*Lorentzen*, 2000; *Fang et al.*, 2004]. Ionization caused by proton or hydrogen impact on atmospheric neutral species leads to emissions from the same excited population that is created by electron precipitation [*Ivchenko et al.*, 2004b; *Galand and Lummerzheim*, 2004]. Protonoelectrons produced through ionization and stripping collisions also contribute to excitation of atmospheric species [*Strickland et al.*, 1993; *Lummerzheim et al.*, 2001; *Galand and Lummerzheim*, 2004] and, to a lesser extent, to ionization [*Basu et al.*, 1987; *Galand et al.*, 1999; *Simon et al.*, 2007]. It is critical to separate the electron and proton components of the precipitation. Assuming pure electron precipitation may lead to misinterpretation of auroral brightnesses in terms of ionospheric parameters such as ionization rate and conductivity [*Galand et al.*, 2002; *Galand and Lummerzheim*, 2004].

[3] On the large-scale, electron and proton induced auroral ovals often overlap [*Burch et al.*, 2001]. However, protons can be the dominant energy source in the cusp and at the equatorward boundary of the duskside auroral oval [*Creutzberg et al.*, 1988; *Hardy et al.*, 1989; *Galand et al.*,

[1]School of Physics and Astronomy, University of Southampton, Southampton, UK.
[2]Center for Space Physics, Boston University, Boston, Massachusetts, USA.
[3]Department of Physics, Imperial College London, London, UK.
[4]Space and Plasma Physics, School of Electrical Engineering, KTH, Stockholm, Sweden.
[5]Geophysical Institute, University of Alaska Fairbanks, Fairbanks, Alaska, USA.

0148-0227/11/2011JA016474

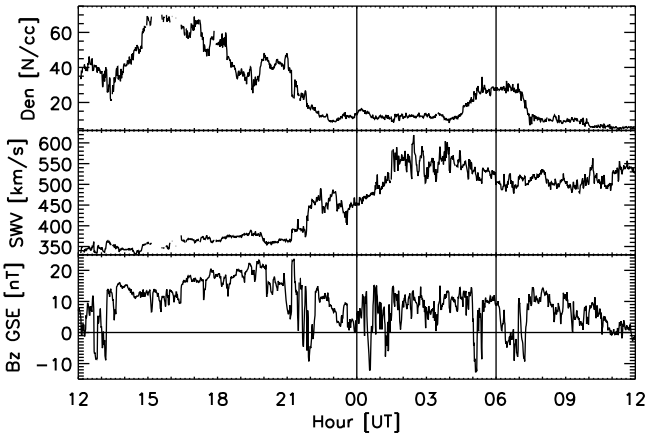

Figure 1. Solar wind parameters from Geotail 15–16 December 2001. From top to bottom: ion density, solar wind speed, and B_Z. The events described in this paper occurred between 00:00 and 06:00 UT, as highlighted with vertical lines.

2001]. *Lummerzheim et al.* [2001] found that an increase in the blue wing of the Balmer lines, rather than a shift in the peak wavelength, is more indicative of an increase in proton energy. Observations from Svalbard of H Balmer profiles at high spectral resolution have allowed changes in energy input to be determined [*Deehr et al.*, 1998; *Lanchester et al.*, 2003b]. *Galand et al.* [2004] measured H α and H β from Tromsø, Norway, on the equatorward edge of the evening auroral oval where more energetic protons precipitate. The blue wing observed is larger than that observed from Svalbard. The advances made in the study of proton aurora both in ground-based observations and modeling in recent decades are well summarized by *Galand and Chakrabarti* [2006]. *Simon et al.* [2007] have used a numerical kinetic-fluid code which couples proton and electron precipitation effects. They used input from an overpass of the DMSP F13 satellite near Svalbard to compare their model results with measurements of H α from the ground at Longyearbyen, Svalbard, and to study the relative effects of collisions and magnetic mirroring of protons on the model profiles.

[4] In the present study ground-based measurements from 16 December 2001 have been used to determine how the emissions from protons and electrons are related and whether they match the particle fluxes measured by satellites. *Ivchenko et al.* [2004b] have studied emissions measured on the previous day, and found enhanced brightness of the multiplet O^+ ^4P-^4D relative to that of N_2^+ 1N (0, 2). It was shown that proton precipitation was the dominant source of both emissions, with enhanced O^+ intensities from proto-ionization. That event occurred at a time of low solar wind velocity and high solar wind density, whereas the events studied in this paper occurred during high solar wind speed and low density. The present events have a greater flux of electrons than that of the previous day, which was almost pure proton precipitation.

2. Instrumentation and Data

[5] Observations of H β emissions at Longyearbyen, Svalbard (78.203°N, 15.829°E geographic coordinates) were made with the High Throughput Imaging Echelle Spectrograph (HiTIES) [*Chakrabarti et al.*, 2001; *Galand et al.*, 2004], which is the main instrument on the Spectrographic Imaging Facility (SIF) [*McWhirter et al.*, 2003; *Lanchester et al.*, 2003a]. Light from an 8° slit is collimated, diffracted by an echelle grating, and reimaged on the detector. The slit was aligned with the magnetic meridian and centered on the magnetic zenith. Overlapping diffraction orders are separated by a mosaic of interference filters. For the present data the mosaic included the H β spectral window and two filters to measure the N_2^+ 1N (1, 3) and (0, 2) bands between 463.5–466.0 and 469.0–471.5 nm, respectively. Three lines of a multiplet of O^+ are measured in the passband of the filter for the N_2^+ 1N (1, 3) band. The emission O^+ 464.91 nm overlaps the (1, 3) band head (465.18 nm), but by fitting a synthetic spectrum to the 1N band, the two features can be separated [*Ivchenko et al.*, 2004a]. The detector used during these observations was the Microchannel Intensified CCD [*Fordham et al.*, 1991]. It is a photon counting detector, with very low dark count rate and no readout noise. The spectral resolution of the spectrograph is determined by the slit width, which requires a compromise with the amount of light that enters the instrument. In these observations the spectral resolution is 0.08 nm for the FWHM instrument function. Typical integration times are 10–60 s. Measurements can be integrated over different sections of the meridian slit as required. In the present measurements, time resolution of 62 s was used, including a 2 s readout time, and 60 s integration was performed over the central 2° of the slit.

[6] Height profiles of electron density, electron and ion temperatures and line-of-sight velocities in the ionosphere were obtained with the European Incoherent Scatter (EISCAT) Svalbard Radar (ESR) which is situated 7 km from the optical station (Nordlysstasjonen). The present observations were made with the 42 m antenna pointed along the local magnetic field line. The field of view has half width of 1.3°. The radar program (TAU0) is an alternating code experiment with two 960 μs pulses (15 μs × 64 bits) with range 100–1000 km. An integration time of 6.4 s was used in the experiment. In order to increase the signal-to-noise ratio, preanalysis integration of 64 s and 128 s was made in the present work.

[7] Coincident particle data have been used from the Space Environment Monitor-2 (SEM-2) on the Advanced TIROS-N (ATN) NOAA 16 polar orbiting meteorological satellite, launched in March 2001, in a Sun-synchronous orbit at an altitude of 850 km. We used particle data from two separate SEM-2 sensors: the Total Energy Detector (TED) and the Medium Energy Proton/Electron Detector (MEPED). The TED [*Evans and Greer*, 2000] detects protons and electrons with energies from 50 eV to 20 keV and MEPED [*Codrescu et al.*, 1997] measures electrons from 30 to 1000 keV and protons from 30 to 6900 keV. An ion energy spectrum from DMSP F14 has also been used for comparison [*Hardy et al.*, 1984].

[8] The large-scale temporal and spatial variations of H emissions in the auroral oval have been obtained from the Spectrographic Imager (SI12)/FUV instrument on the Imager for Magnetopause-to-Aurora Global Exploration (IMAGE) satellite in a polar orbit, which provides 5–10 s images of the Doppler-shifted integrated Lyman α emission at 2 min intervals of the entire auroral oval [*Mende et al.*, 2000]. This

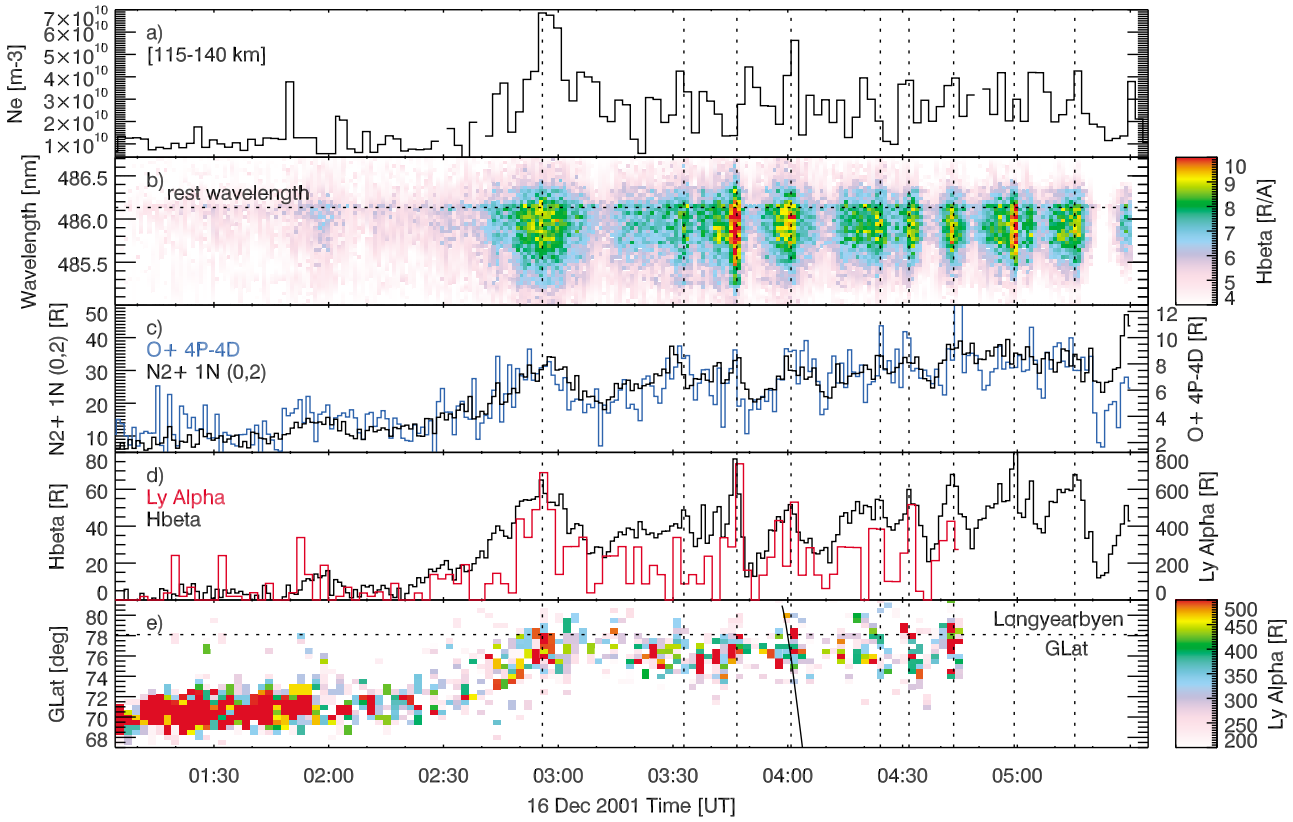

Figure 2. Overview of ground-based measurements for 01:00–05:30 UT on 16 December 2001: (a) ESR averaged electron density between 115 and 140 km, (b) HiTIES H β brightness as a function of wavelength, (c) HiTIES N_2^+ and O^+ integrated brightness, (d) IMAGE Ly α brightness over Svalbard and integrated HiTIES H β, and (e) IMAGE Ly α brightness as a function of geographic latitude. The NOAA 16 track is seen at 04:00 UT. The vertical lines correspond to peaks in the HiTIES integrated H β brightness. The SI12 data do not extend to the end of the interval.

emission, like the Doppler-shifted H β emission, is produced solely by proton precipitation into the atmosphere.

3. Observations

[9] The solar wind conditions for 24 h from noon on 15 December 2001 are shown in Figure 1. Measurements are from the Geotail spacecraft at 20 R_E in GSE X direction and −20 R_E in GSE Y direction (on the dawnside). At 14:00 UT on 15 December the ion density increased from 30 cm^{-3} to 80 cm^{-3}, then decreased to quiet levels of 10 cm^{-3} over the next 8 h. Following the drop in density at 22:00 UT, the solar wind velocity increased from 400 to 550 km s^{-1} over the next 4 h and remained at this large value for about 18 h. At the time of the main observations discussed below, between 00:00 and 06:00 UT on 16 December as indicated in the plot, the density was low and the velocity was high. During the 12 h preceding this interval, the B_Z component of the IMF was strongly positive for many hours. A brief negative excursion at about 01:00 UT was followed by an interval of positive B_Z until 05:00 UT. The components of magnetic field and velocity, B_X and V_X, respectively, oscillated significantly during this time (not shown).

[10] Following the large change in the solar wind density on 15 December at 14:00 UT as measured by Geotail, there was a sudden onset of emissions resulting from proton precipitation measured on the ground at Longyearbyen. This precipitation continued from 15:00 UT to 19:00 UT. At 17:02 UT there was a pass of the DMSP F14 spacecraft close to Longyearbyen. This pass has been analyzed in detail by *Ivchenko et al.* [2004b]. Between 19:00 UT on 15 December and 02:30 UT on 16 December there was very little activity in both the ionosphere above the radar and in optical emissions measured by HiTIES.

[11] For the interval 01:00–05:30 UT on 16 December, the radar and optical data measured from the ground over Longyearbyen are shown in Figures 2a–2c. Figure 2a is the electron concentration averaged between heights of 115 and 140 km. Figure 2b shows the brightness of the Doppler-shifted H β profiles as wavelength versus time. In Figure 2c are emissions recorded by the HiTIES spectrograph, integrated over appropriate wavelengths; the N_2^+ (0, 2) emission has been integrated over the P branch and multiplied by a factor of 2 to include the R branch, and the O^+ ^4P-^4D multiplet brightness has been estimated by using the brightest line embedded in the N_2^+ 1N (1, 3) band. The start of the main precipitation is close to 03:00 UT, with a sequence of increases in all emissions, and corresponding increases in electron density at most times. The peaks in integrated H β brightness have been highlighted with vertical dashed lines. Just before 05:30 UT, there is an increase in the N_2^+ emissions which is an indication of more energetic electron

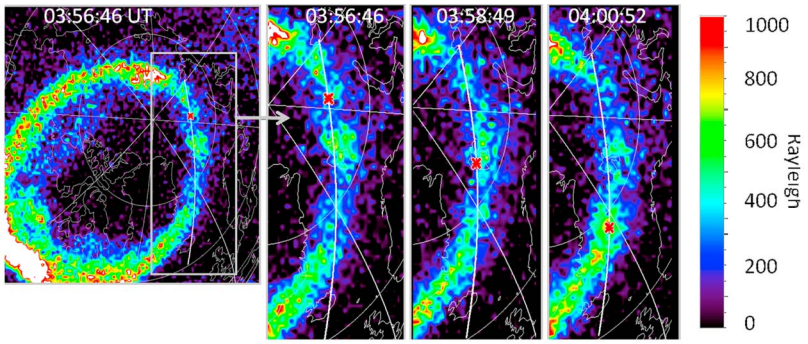

Figure 3. IMAGE Ly α images of the auroral oval in geographic coordinates at times 03:56:46, 03:58:49, and 04:00:52 UT with NOAA 16 footprint and position (red stars) at each time. Svalbard lies under the NOAA 16 position at 03:58:49 UT.

precipitation. Figures 2d and 2e include the Ly α emission measured by SI12 from above. Figure 2d compares the variation in Ly α over Longyearbyen with the H β brightness integrated over the Doppler profile (484.4–487.5 nm). Similar variations are seen in H β from the ground and Ly α from space, despite the difference in spatial resolution. Figure 2e is discussed below. Conditions during the interval studied were hazy, with a thin covering of cloud. These conditions will reduce the intensities in the field of view of the optical instruments through increased extinction, and will also scatter emissions from outside the instrument field into their apertures [*Gattinger et al.*, 1991].

[12] The Ly α images from which the line plot in Figure 2d was derived provide an overview of the changes occurring in the auroral oval as a result of the changes in the solar wind properties. Sections of three consecutive images in Ly α measured by the SI12 detector on the IMAGE spacecraft are shown in Figure 3, as well as a sample image of the whole oval at the time of a pass of NOAA 16 over Svalbard; the NOAA 16 track and foot point for an assumed height of the emission at 120 km are marked in each frame by a white line and red star, respectively. Svalbard is under a region of bright emission in the first frame, and almost coincident with the foot point in the second frame.

[13] The relative positions of the main instruments used in the analysis are shown in Figure 4. The footprint of NOAA 16 at 120 km is shown in 2 s intervals with bold crosses corresponding to full minutes. The locations of HiTIES and ESR are marked with a diamond and a triangle, respectively, and their locations traced up the magnetic field at 120 km are similarly marked to the south. The closest approach of NOAA 16 footprint to the HiTIES measurements occurs at about 03:58:50 UT when the spatial separation is of the order of 70 km.

[14] The change in shape and position of the auroral oval relative to Longyearbyen during the interval 01:00–04:45 UT is seen in Figure 2e, which is a time series of meridional slices from the SI12 images. The data have been integrated over 1° in longitude centered on 15.3 E. At about 02:30 UT the region of Ly α emission moves to higher latitudes, with a peak in emission intercepting the latitude of Longyearbyen at 02:50 UT. The NOAA 16 footprint has been added as latitude versus time in Figure 2e, to indicate the time at which the satellite encountered proton aurora, and the time of its closest approach to the latitude of Longyearbyen. Figures 2b, 2d, and 2e confirm that the proton aurora is very variable in both space and time in the dawnside region over Svalbard, forming in blob-like regions. The emissions extend poleward in bursts (Figure 2e), which correspond to either the movement or formation of a blob. The temporal resolution of the IMAGE data (2 min) renders it impossible to differentiate between the two.

[15] The NOAA 16 particle data are plotted in Figure 5 as a function of both time (lower abscissa) and magnetic latitude (upper abscissa). Figure 5 (top) shows the electron (blue lines) and proton (red lines) energy flux from the TED at both 2 s (thin lines) and 16 s (thick lines) resolution. The vertical black bars at 03:59 UT are an estimate of the uncertainty in the measurements. Figure 5 (bottom) is the mean

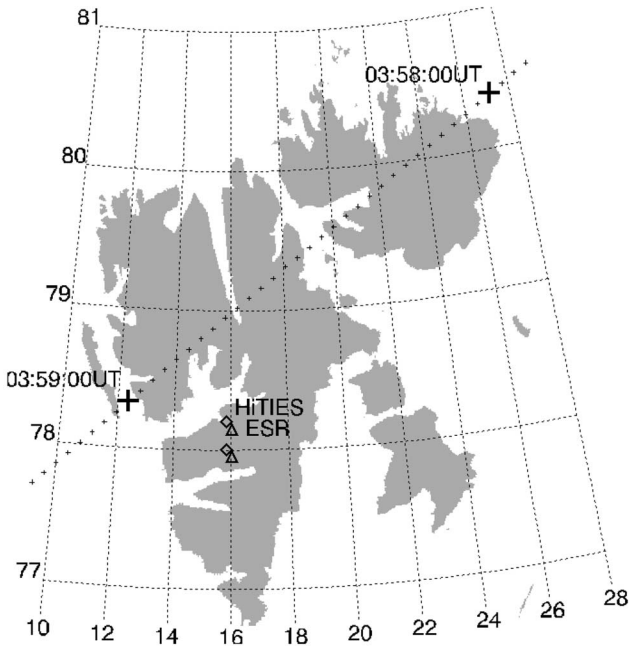

Figure 4. Relative positions of the ground-based instruments and the NOAA 16 footprint in 2 s intervals traced to 120 km over Svalbard in geographic coordinates. The ground locations of HiTIES and ESR are marked. The lines of sight at 120 km for both instruments are indicated by secondary symbols in the southward direction.

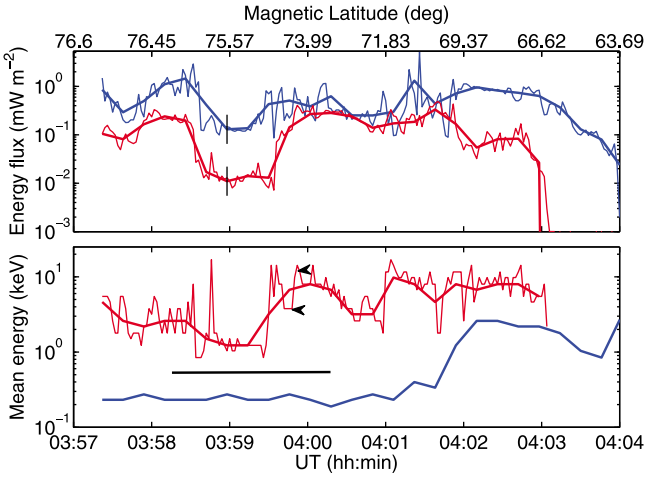

Figure 5. TED mean energy and energy flux for protons (red) and electrons (blue) for 2 s (thin lines) and 16 s (thick lines) averages from the NOAA 16 satellite. Time of closest approach to Longyearbyen is at 03:58:50 UT. The horizontal bar covers data which could represent the variable ground measurements.

energy for electrons at 16 s (2 s not available), and protons at both 2 s and 16 s resolution. For the first part of this interval (up to 04:01 UT) a probable source region is the dayside extension of the boundary plasma sheet (BPS), with electron energies of a few 100 s of eV, and ion energies greater than 1 keV, rising to at least 10 keV [*Newell and Meng*, 1992]. The energy fluxes of electrons and ions show some blob-like variations in the 16 s data in this region. At 04:02 UT the electron mean energy increases as the satellite travels to lower latitudes and MLT, where the source region is likely to be the central plasma sheet (CPS). Note the separation in the electron and proton precipitation regions, with the electron oval more equatorward by 3° as expected in the morning sector. The closest approach of the satellite footprint to Longyearbyen is at 03:58:50 UT, when it reached the magnetic latitude of 74.9°, which corresponds to 06:16 MLT. The horizontal bar in Figure 5, roughly centered on the time of closest approach, represents times when the particle data could be chosen to model the aurora measured over Longyearbyen. The two arrows mark the mean energies that are used as first input values for the modeling described in section 4. They were chosen to represent times of increasing flux and mean energy, and to coincide with a brighter region of emission. Choosing the time at which the NOAA 16 data best represent the ground data needs careful consideration. These choices are discussed further in section 5.

4. Comparison of Observations and Model Results

4.1. Method

[16] One of the aims of the present work is to reproduce by modeling the changes to emissions from both electrons and protons and to use these to confirm that the input spectra used in the modeling is realistic.

[17] There appear to be strong correlations between the changes in E region electron density and H β brightness, as well as with the other emission brightnesses. By matching the resulting model emission brightnesses induced by the incident protons and electrons with those measured by HiTIES, and comparing the model electron density profiles with those measured, we can confirm the relative contributions to emissions and ionization from all contributing processes.

[18] The flowchart of Figure 6 describes the logic behind the analysis that has been performed. The model components are shown in the gray shaded box, and include a proton transport code [*Galand et al.*, 1997], an electron transport code [*Lummerzheim and Lilensten*, 1994], and a time-dependent ion chemistry model [*Palmer*, 1995; *Lanchester et al.*, 2001]. Both transport codes, which describe the transport and energy degradation of suprathermal particles, require incident energy spectra (shown as white boxes). All measured quantities are shown as blue shaded boxes, with those used as direct input at the top, and those compared with model results at the bottom. Model results are shown as ovals; dashed lines lead from the proton transport to H β emission profiles and spectral shape, and from both transport codes to emissions from N_2^+ and O^+. The ion chemistry produces electron density height profiles. Black thick connectors show where the results are compared with measured values, both emissions and electron densities. There are several feedback loops (blue arrows) which are used to inform the choices of input. The latter checks are a necessary part of the analysis because of the spatial and temporal uncertainties associated with the coincidence of the NOAA 16 spacecraft and the ground measurements.

4.2. Input Spectra

[19] For the incident proton and electron spectra, the NOAA 16 particle data shown in Figure 5 do not give a full energy spectrum, but a mean energy and total energy flux, from which a spectrum must be constructed. The curves in Figure 7 are several different input spectra used for testing the model. The curves labeled NOAA 1 and NOAA 2 are spectra constructed from NOAA 16 proton data at the times shown by arrows in Figure 5. They are associated with mean energies of 3.8 and 12.0 keV, respectively, and total energy fluxes of 0.13 and 0.30 mW m^{-2}, respectively. A correction factor has been applied to take into account the limited spectral coverage of TED (50 eV to 20 keV). The distribution in energy is assumed to be a Maxwellian over the whole spectral range for NOAA 1 and below 20 keV for NOAA 2. For the latter, there are enough counts in MEPED (>30 keV) to infer a high-energy tail, assumed to be a power law as described by *Fang et al.* [2007]. The dashed curve is similarly a Maxwellian shaped spectrum based on the electron data, with a power law extension below 50 eV. It has a mean energy of 250 eV and total energy flux of 1.0 mW m^{-2}. Included in Figure 7 is the DMSP F14 measured proton spectrum from 15 December 2001 with a mean energy of 2.3 keV (with peaks at 1 keV and 8 keV), and total energy flux of 0.4 mW m^{-2}. All of these energy spectra have been used as input to the modeling. MSIS is used for defining the neutral atmospheric densities. Conditions on 16 December were as follows: Ap = 10, f10.7 = 209, mean f10.7 = 194.

[20] The proton transport model produces the Doppler shifted H β profile resulting from each input spectrum. The profiles labeled NOAA 1 and NOAA 2 in Figure 8 are the results of model runs for the NOAA 1 and NOAA 2 spectra

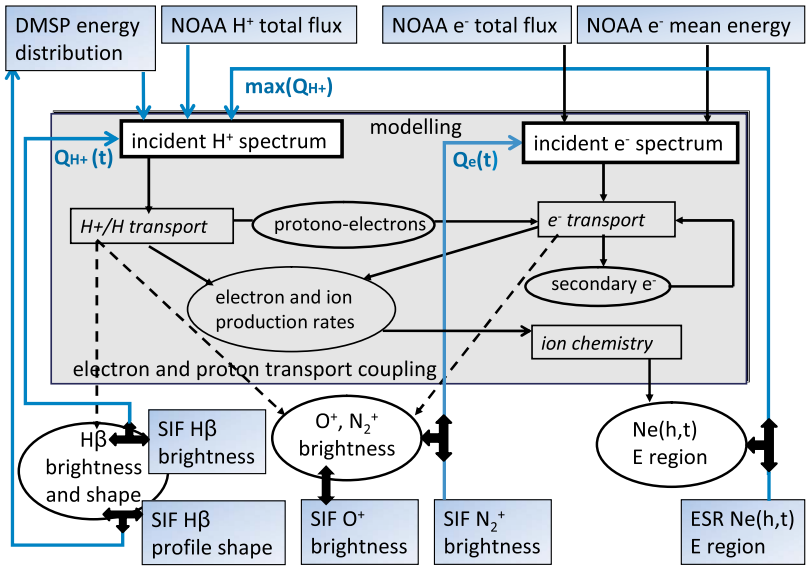

Figure 6. Flowchart to describe the inputs and outputs to the ionospheric model (gray box) and the comparison between measurements (blue boxes) and modeled quantities (ovals). Blue lines show resulting feedback made on the choice of input spectra.

of Figure 7. They have been normalized to the peak of the measured profile shown in black (not the unshifted peak, which is the result of geocoronal emission). Figure 8 shows that the peak is not a good proxy for the energy of the incident protons. The maximum shift of the peak at 485.4 nm corresponds to field aligned H atoms of 1 keV. This is because for energies below 10–20 keV the beam is predominantly made of neutral H atoms and the H β excitation cross section between N_2 and H peaks near 1 keV. The shapes of the H β modeled profiles derived from NOAA 16 particle input are not a good fit to the observations for the blue-shifted wing, particularly for NOAA 2, indicating that the Maxwellian (or close to Maxwellian) distribution in energy is most likely underestimating the contribution of low-energy protons. The red curve is the model profile using the DMSP measured spectrum, and as a result of the increase in low-energy flux (as illustrated in Figure 7), makes a much better fit to the data. Therefore, the shape of the DMSP input spectrum has been used in the following analysis, as indicated in Figure 6 by the blue arrow leading from the SIF H β shape through the DMSP energy distribution to the input H^+ spectrum. It has the advantage of being a measured spectrum with a realistic contribution from low-energy protons.

[21] In order to obtain the best fit to the electron densities in the *E* region, the total proton energy flux is a key factor. The electron density is affected not only by precipitating electrons, but also by precipitating protons, and induced energetic H atoms and protonoelectrons. The proton model provides the ionization rate by protons and H atoms, and also the source function of the protonoelectrons, used as input

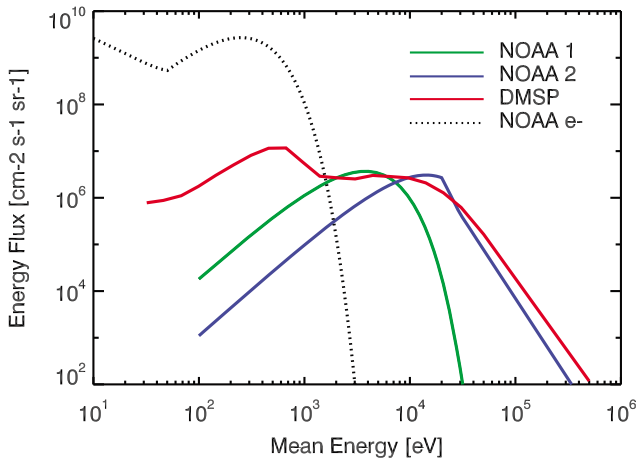

Figure 7. Input spectra constructed from NOAA particle data and measured DMSP spectrum.

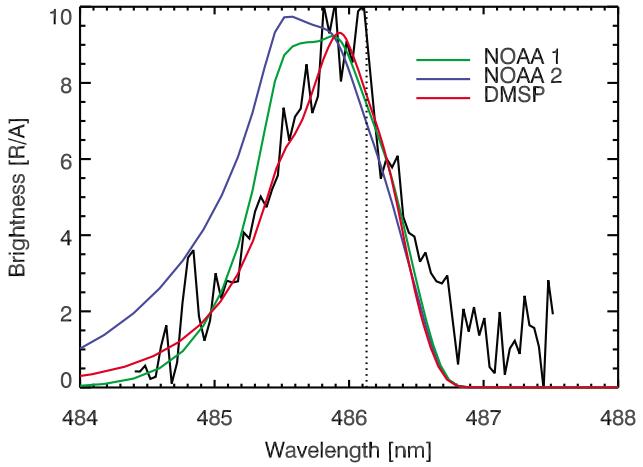

Figure 8. Modeled Doppler-shifted profiles of H β using as input the proton spectra in Figure 7 compared with measured profile in black. Normalization has been applied to the modeled spectra.

for the electron transport model. The changes in measured H β brightness are indicative of the temporal changes in the incident H^+ energy flux during the increase at the time close to the NOAA 16 pass, centered on 04:00 UT. The blue arrow labeled Q_{H+} (t) in Figure 6 represents this input to the H^+ spectrum. A starting value of the total flux is taken from the NOAA 16 H^+ data, and then a range of values is applied, using the same shape and temporal changes. The ion chemistry model driven by the ion production rates from the proton and electron transport models provides electron densities which can be compared with those measured from the ESR. A maximum energy flux for the incident protons is derived from this comparison. It corresponds to the energy flux which yields a best fit between the modeled and the observed electron density profiles in the 115–140 km height range, which includes the *E* region enhancement (blue arrow labeled max(Q_{H+}) in Figure 6).

[22] The above sequence for proton input spectra is summarized as (1) the energy distribution is based on DMSP (justified by the comparison with H β Doppler-shifted profile), (2) the energy flux temporal variation is based on H β brightness variability, (3) the energy flux absolute value is first based on NOAA 16 energy flux, and then (4) a range of values is used to find the best fit of modeled and observed electron densities between heights 115–140 km.

[23] In a similar way, the electron input spectra have been determined. The shape of the electron input spectrum is shown in Figure 7, constructed from NOAA 16 particle data set. From Figure 5 it is seen that the mean energy of electrons remains constant at around 250 eV throughout the event. However, the electron flux shows the same blob-like variations as the proton flux. Again it is necessary to estimate the temporal variations of electron energy flux to match the conditions measured on the ground. In this case we have used the measured N_2^+ 1N (0, 2) brightness. It is an approximation as it is not produced by electrons only. This feedback loop is shown in Figure 6 as the blue arrow from SIF N_2^+ brightness labeled Q_e(t). The starting value for total flux is taken from the NOAA 16 electron data.

4.3. Results

[24] Several of the temporal blobs in H β emission and electron density seen in Figure 2 have been analyzed, but only one is presented here in detail. The results from the increase seen at the time of the NOAA 16 pass close to 04:00 UT are shown in Figure 9. The measured ESR electron density is shown in Figure 9a at both 1 min and 2 min resolution (solid and dotted black lines) integrated between heights 115–140 km. Figure 9a also contains three sample model results of the electron density (gray solid lines), using values of max(Q_{H+}) of 0.30, 0.20, and 0.10 mW m^{-2}. These values have been chosen from NOAA 16 data in Figure 5 for which 0.30 mW m^{-2} is the maximum measured value. Temporal changes determined by the H β integrated brightness are shown by the black line in Figure 9b. The gray lines in Figure 9b are modeled H β brightness without extinction. Figure 9c shows the measured H β spectral profiles. Figure 9d shows the variation with time in measured N_2^+ 1N (0, 2) and O^+ multiplet. Figure 9e shows the Ly α emission from above as a function of geographic latitude, with the latitude of Longyearbyen marked with a dotted line. It confirms that the time of closest approach over Longyearbyen at 03:59 UT corresponds to the drop in flux and mean energy seen in Figure 5 at the same time.

[25] It can be seen from Figure 9a that the maximum value of the proton flux from NOAA 16 of 0.30 mW m^{-2} produces excess electron density at the peak relative to the measured *E* region density. The closest fit of the modeled electron density to the measurement at the peak near 04:00 UT corresponds to a maximum proton energy flux of 0.23 mW m^{-2}. The lack of a good fit to the temporal changes in electron densities is discussed in section 5. In Figure 9b a comparison of the measured H β with absolute values from the model provides an estimate of extinction at the time. By comparing the measured H β brightness at 04:00 UT with the H β brightness obtained with a proton energy flux of 0.23 mW m^{-2}, which best fits the observed electron density, we derive an extinction of about 2.8.

[26] The measured electron density height profile (60 s integration) at the peak of the event at 04:00 UT is compared with the model results in Figure 10. Measured values are shown as crosses, and the total modeled profile as a black line. The various contributions to the model profile are as follows: ionization by protonoelectrons (dash-dotted line), ionization by H^+ and H (dash-triple dotted line), total ionization from the proton beam (long-dashed lines) and total ionization from precipitating electrons (dot lines). For this particular energy distribution, which has a large contribution from soft proton precipitation, the ionization resulting from protonoelectrons is small. The horizontal lines mark the heights between which the integration was made in order to fit the peak of the profile resulting from proton precipitation. The effect of the electron input flux on the *F* region densities is demonstrated with two model outputs shown as dotted profiles. The curve corresponding to a lower electron density profile (blue dots) is from a constant 0.5 mW m^{-2} total energy flux, which greatly underestimates the observed *F* region peak (solid blue). The total curve peaking close to 2×10^{11} m^{-3} corresponds to an electron peak energy flux of 3.0 mW m^{-2}, which is the one adopted as the best fit. Auroral soft electrons drive the *F* region peak, while auroral protons drive the *E* region peak, confirming earlier findings by *Vontrat-Reberac et al.* [2001] and *Simon et al.* [2007]. Problems related to the fitting of the upper *E* region and *F* region are discussed in section 5.

[27] Table 1 summarizes the results of the comparison between all measured and modeled emissions at the time of the peak at 04:00 UT. Proton precipitation is the sole source of H β. Proton transport modeling produces 143 R in comparison to 51 R measured, with extinction being the likely cause of the difference. Both electron and proton precipitation contribute to N_2^+ 1N. The (0, 2) vibrational band was modeled as 88 R with 76 R from electron precipitation, 10 R from ionization by protons and H atoms and 2 R from ionization by protonoelectrons. The observed integrated band brightness was 30 R, resulting in an estimate of extinction of 2.9. The O^+ multiplet was modeled as 27 R with 26 R coming from electron precipitation, and the remainder coming from ionization by H/H^+. Protonoelectrons provide an insignificant contribution. In this case the deduced extinction is 3.0. The estimated electron energy flux of 3.0 mW m^{-2} is supported by the emission features it produces. The lower flux of

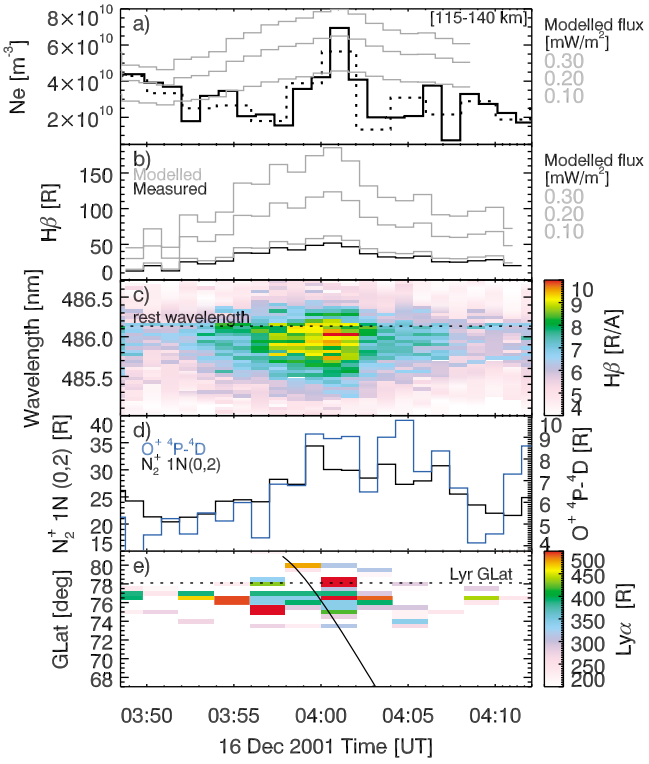

Figure 9. Blowup plot of the event centered at 04:00 UT: (a) measured (black solid lines, 60 s; dotted lines, 120 s) and modeled (gray lines) electron density between 115 and 140 km as a function of modeled proton flux. (b) Modeled and measured H β integrated brightness as a function of flux excluding extinction. (c) Measured H β as a function of wavelength and brightness. (d) Height-integrated N_2^+ 1N (0, 2) and O^+ ^4P-^4D brightness. (e) Ly α emission and NOAA 16 pass as a function of geographic latitude.

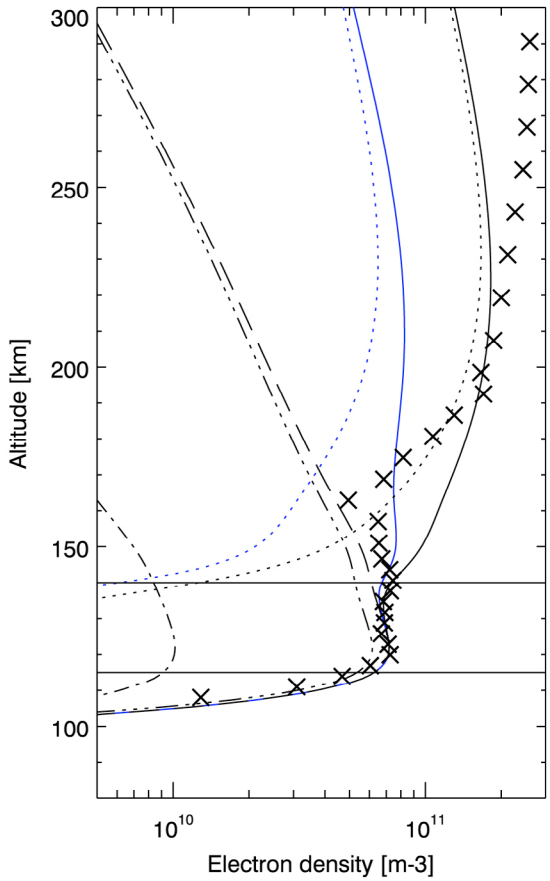

Figure 10. Measured (crosses) and modeled ESR electron densities at the time of the peak ionization at 04:00 UT. Model electron precipitation (dotted lines) is shown for two different peak input energy fluxes of 0.5 (blue) and 3.0 mW/m^2 (black). Other contributions are protonoelectrons (dash-dotted line), protoionization (dash–triple dotted line) and total proton ionization (long-dashed line). The solid lines correspond to total modeled electron densities.

0.5 mW m^{-2} would give electron induced emissions of magnitude similar to the proton induced N_2^+ 1N and O^+ emissions, which is not what is observed.

[28] The measured optical emissions of N_2^+ 1N and O^+ for the event at 04:00 UT are shown in Figure 9d. In all the events (or blobs) studied, the correlation between the two emissions suggests a dominant excitation mechanism, in this case electrons (see Table 1). This result is confirmed by the agreement between the measured and modeled emissions, and the values of extinction obtained in all emissions. Therefore, the modulation in all measured emissions is found to be the result of a modulation in both proton and electron fluxes, which is seen in NOAA 16 data, and confirmed by modeling.

5. Discussion

[29] The events described allow a quantitative analysis of the sources of emissions and ionization resulting from both proton and electron precipitation, using input parameters determined from the NOAA 16 satellite. Some checks have been made to the input to provide the closest estimate of the precipitating particle mean energy and energy fluxes, taking account of the close, but not perfect, conjunction of NOAA 16 with the ground site (though closer than 100 km), and the temporal and spatial changes as the satellite passed. An exact coincidence of in situ data and ground data is rare; although there are some uncertainties in the interpretation of the spatial and temporal changes in the proton aurora (i.e., both Balmer H β and Ly α), by combining all available data with modeling, the ionospheric effects of both protons and electrons have been determined.

[30] The values for energy fluxes and mean energies at the top of the ionosphere given in Table 2 are derived for the

Table 1. Measured Emission Brightnesses From the HiTIES Spectrograph Compared With Modeled Emission Brightnesses From Proton and Electron Precipitation, With Energy Fluxes of 0.23 and 3.0 mW/m^2, Respectively

Brightness (R)	H β	N_2^+ (0, 2)	O^+
Measured	51	30	9
Modeled protons/H	143	10	1
Modeled electrons	-	76	26
Modeled protonoelectrons	-	2	0
Total without extinction	143	88	27
Implied extinction	2.8	2.9	3.0

Table 2. Derived Energy Fluxes and Mean Energies at the Peak of the 04:00 UT Event

	Protons	Electrons
Energy flux (mW/m^2)	0.23	3.0
Mean energy (keV)	2.5	0.25

time of the peak of the event measured on the ground. All of these values are in agreement with measured particle data from NOAA 16 (Figure 5) at the peak of the increase in energy flux starting at 03:58 UT in the NOAA 16 data. For the ground data, this time corresponds to the "temporal blob" measured by HiTIES which began at about 03:57 UT and peaked at 04:00 UT (see Figure 9). As seen in the first two images of Figure 3, IMAGE measures this blob over Svalbard and NOAA 16 intercepts it before its closest approach to the ground station. The third image of Figure 3 shows that by 04:00 UT, NOAA 16 is entering a brighter blob which is far to the west of Svalbard. This result confirms that the NOAA 16 data at the times of the arrows in Figure 5 were not coincident with the ground data and were of higher mean energy (3.8 and 12 keV) than the blob measured on the ground at this time, with slightly greater energy flux at the peak (0.3 mW m^{-2}). The above interpretation is supported by Figure 9e.

[31] Because of the structure seen in the H β emissions, and in the precipitation, the fields of view of both HiTIES and the radar may not be uniformly filled at all times. Also the 7 km separation of the instruments could account for some distinct differences between the variations in electron density and H β seen in Figures 2a and 2b, for example at 03:45 UT. The changes in electron density seen in Figure 9a are very abrupt at times and the ESR height profiles are unusually variable at 1 min resolution. The spatial displacement of precipitation out of the field of view will not produce a sudden drop in electron density, and hence the model densities show a smooth time variation. The abrupt changes in the measured profiles can be explained by the presence of horizontal electric fields, which affect the movement of plasma in and out of the radar beam at heights around 130–140 km where ion mobility is high [*Lanchester et al.*, 1998]. There is indeed evidence that electric fields were affecting the ionosphere over Svalbard. The ion temperatures measured by the radar are variable, with peak values of 2000 K in the *E* region and 5000 K in the *F* region. Enhancements in field-parallel ion temperature can be translated into a velocity difference between ions and neutrals [*Lockwood et al.*, 1993; *McCrea et al.*, 1993] and consequent horizontal electric fields. Added to this evidence are measurements from ground magnetometers and the Cutlass radar (M. Lester, private communication, 2011) that show significant wave activity present over Svalbard. We also note that the Geotail data show a strong oscillatory signature in the solar wind V_X and B_X components.

[32] Another feature of this event is that electron and proton fluxes are modulated together in the NOAA 16 data (and in the model results). These so-called blobs are interpreted as spatial regions from NOAA 16 data because of the satellite speed; the HiTIES data imply that either the emissions are increasing and fading in one place, or they are moving in and out of the field of view. However, the mean energies of the electrons are not modulated, but remain very steady at around 200–300 eV. The latitudinal variation of Ly α seen in Figure 2e indicates that the blobs are northward extensions of a wider region of proton precipitation, and that Longyearbyen is in the most poleward part of the emission region. It is possible that there is a spatial variation in energy within these extensions, which could be interpreted as an energy filter effect, with energy dispersion of ions and not electrons. *Deehr et al.* [1998] and *Sigernes* [1996] have studied similar events with spectral measurements of H β profiles, where the changes in energy with latitude depend on the direction of convection and changes in the solar wind direction. *Lorentzen and Moen* [2000] have used NOAA12 data passing north of Longyearbyen, in conjunction with optical measurements on a larger scale, to study the possible source regions of the precipitating particles. Their data are in good agreement with the assumption that the source of particles in our event is the dayside extension of the BPS; similar values of mean energy and total energy flux for both protons and electrons are measured by NOAA12. The origin of the modulations in the energy fluxes and proton energies on 16 December 2001 is part of a separate study, to determine whether the modulations are related to the oscillations seen in the solar wind, and whether they in turn are related to the wave activity measured on the ground and in the ionosphere. That study will investigate the large-scale changes associated with proton precipitation events [e.g., *Lorentzen and Moen*, 2000; *Lockwood et al.*, 2003; *Fuselier et al.*, 2004, 2007; *Meurant et al.*, 2004], whereas the present study is of the ionospheric response to both auroral electrons and protons in a particular event.

[33] A comparison can be made with data from the previous day (15 December) at 17:02 UT [*Ivchenko et al.*, 2004b]. The value of extinction of about 2.5 for H β compares well with that of 2.8 derived here for similar hazy conditions. *Lummerzheim et al.* [1990] estimated an atmospheric extinction coefficient for clear conditions to be 1.49, so a further factor of 1.9 is needed, which is reasonable for the present conditions of thin cloud cover. The agreement between estimates for extinction from all emissions is good. The main difference between the two sets of observations is that in the present event the ratio of the O^+ multiplet to N_2^+ is between 0.2 and 0.3. On the previous day the ratio was close to unity because of enhanced O^+ relative to N_2^+ in almost pure proton precipitation. The electron flux measured by DMSP F14 on the previous day was less than 0.1 mW m^{-2} although the mean energy of electrons was very similar. Note that the total flux of electrons is 30 times greater in the present event. This enhancement in O^+ seen on the previous day is yet to be reproduced by modeling, although *Ivchenko et al.* [2004b] proposed that the lack of agreement was the result of severe underestimation of the O^+ emission cross section by low-energy proton impact. For comparison, a typical ratio of O^+ multiplet to N_2^+ in electron aurora was found to be close to 0.1 by *Ivchenko et al.* [2004a]. From modeling, this ratio can be as high as 0.5 for low-energy electron precipitation and the ratio decreases with increase in energy.

[34] The measured electron density height profiles suffer from having no absolute calibration available. However, we have made a comparison with calibrated data from April 2001, and find no changes to the radar system constant.

Therefore the uncertainty in the densities has been estimated at ±10%. Modeling the auroral ionosphere above 140 km presents several problems, and in the present work we have concentrated on the *E* region between 115–140 km where the effect of protons is dominant. Ionization rates in the *E* region have been estimated to vary by much less than ±10% for conditions such as those observed, with variable electron and ion temperatures. Above 140 km, the value of energy flux chosen for the electron input spectrum has a large effect on the model results. For the profile shown in Figure 10, the electron energy flux value of 0.5 mW m^{-2} underestimates the densities by a factor of about 0.5 in the *F* region, but makes a good fit in the region around 150 km. The maximum value of 3.0 mW m^{-2} makes a good fit at 200 km, but overestimates the densities at heights around 150 km at this time. The latter value is confirmed as a good estimate by the agreement with the optical data, demonstrating the value of such complementary data sets. The present results compare well with those, also from Svalbard, of *Vontrat-Reberac et al.* [2001] and *Simon et al.* [2007], who found the dominant cause of ionization in the *E* region to be precipitating protons, and in the *F* region to be low-energy electrons. However, because there are several uncertainties associated with the *F* region densities and transport effects, we put most weight on the *E* region results.

6. Summary

[35] In the events of 16 December 2001 between 02:00 and 06:00 UT, temporal and spatial modulations of emissions were measured both on the ground and from space. The emissions from nitrogen and oxygen were found to be mostly the result of low-energy electron precipitation in the *F* region, with a small contribution (about 10%) from H^+ and H precipitation. The contribution from protonoelectrons was negligible. Proton precipitation, which is responsible for the Doppler-shifted H β emission, was found to be the main cause of the *E* region ionization.

[36] It was found that assuming a Maxwellian shape for the proton input energy spectra on the basis of the total energy flux and mean energies measured in situ led to greatly underestimating the low-energy proton population, as demonstrated by the shape of the measured Doppler profile. By a careful analysis of the combined data sets, model inputs have been chosen via feedback loops from measured auroral emissions and electron densities (see Figure 6). The resulting values for mean energy and total energy flux (see Table 2) agree well with the values measured by NOAA 16 as it passed through a region of increased hydrogen emission measured by IMAGE, the same region of enhanced emissions and electron densities that was measured on the ground. The source region of the particles is thought to be the dayside extension of the boundary plasma sheet. The cause of the modulations in energy flux of both electrons and protons, and in the mean energies of protons, but not of electrons, is the subject of further investigation.

[37] Although the main interest here is in the *E* region peak, an improved temporal modeling of the local field line flux variation would result in more accurate model electron densities outside the peak density. However, this case study attests to the strong capabilities of using a comprehensive coupled model as an organizing element of in situ particle measurements and ground-based optical observations to interpret the ionospheric measurements.

[38] **Acknowledgments.** O.J. is supported by NSF grant 0940283. M.G. is partially supported by the Science and Technology Facilities Council (STFC) rolling grant to Imperial College London. EISCAT is an international association supported by research organizations in China (CRIRP), Finland (SA), France (CNRS, until the end of 2006), Germany (DFG), Japan (NIPR and STEL), Norway (NFR), Sweden (VR), and the United Kingdom (STFC). We thank the EISCAT campaign team, in particular, Vikki Howells for running the radar experiment and Ian Furniss for essential running of the SIF instruments. We thank Björn Gustavsson and Daniel Whiter for help with the auroral modeling and Ian McCrea for help with analysis of the ESR data. We thank Harald Frey for supplying the IMAGE data. We thank D. Evans for supplying the NOAA 16 particle data, and D. Hardy, F. Rich, and P. Newell for the use of the DMSP particle data. Geotail magnetic field data were provided by T. Nagai through DARTS at the Institute of Space and Astronautical Science, JAXA, in Japan.

[39] Robert Lysak thanks the reviewers for their assistance in evaluating this manuscript.

References

Basu, B., J. R. Jasperse, R. M. Robinson, R. R. Vondrak, and D. S. Evans (1987), Linear transport theory of auroral proton precipitation: A comparison with observations, *J. Geophys. Res.*, *92*, 5920–5932.

Burch, J. L., et al. (2001), Views of Earth's magnetosphere with the IMAGE satellite, *Science*, *291*, 619–624.

Chakrabarti, S., D. Pallamraju, J. Baumgardner, and J. Vaillancourt (2001), HiTIES: A High Throughput Imaging Echelle Spectrograph for ground-based visible airglow and auroral studies, *J. Geophys. Res.*, *106*, 30,337–30,348.

Codrescu, M. V., T. J. Fuller-Rowell, R. G. Roble, and D. S. Evans (1997), Medium energy particle precipitation influences on the mesosphere and lower thermosphere, *J. Geophys. Res.*, *102*, 19,977–19,988.

Creutzberg, F., R. L. Gattinger, F. R. Harris, S. Wozniak, and A. Vallance Jones (1988), Auroral studies with a chain of meridian scanning photometers: 2. Mean distributions of proton and electron aurora as a function of magnetic activity, *J. Geophys. Res.*, *93*, 14,591–14,601.

Deehr, C. S., D. A. Lorentzen, F. Sigernes, and R. W. Smith (1998), Dayside auroral hydrogen emission as an aeronomic signature of magnetospheric boundary layer processes, *Geophys. Res. Lett.*, *25*, 2111–2114.

Eather, R. H. (1967), Auroral proton precipitation and hydrogen emissions, *Rev. Geophys.*, *5*, 207–285.

Evans, D. S., and M. S. Greer (2000), Polar orbiting environmental satellite space environment monitor: 2. Instrument description and archive data documentation, *Tech. Memo. OAR SEC-93*, NOAA, Boulder, Colo.

Fang, X., M. W. Liemohn, J. U. Kozyra, and S. C. Solomon (2004), Quantification of the spreading effect of auroral proton precipitation, *J. Geophys. Res.*, *109*, A04309, doi:10.1029/2003JA010119.

Fang, X., M. W. Liemohn, J. U. Kozyra, D. S. Evans, A. D. DeJong, and B. A. Emery (2007), Global 30–240 keV proton precipitation in the 17–18 April 2002 geomagnetic storms: 1. Patterns, *J. Geophys. Res.*, *112*, A05301, doi:10.1029/2006JA011867.

Fordham, J. L., J. G. Bellis, D. A. Bone, and T. J. Norton (1991), MIC photon counting detector, *Proc. SPIE Int. Soc. Opt. Eng.*, *1449*, 87–98.

Frey, H. U., S. B. Mende, T. J. Immel, J.-C. Gérard, B. Hubert, S. Habraken, J. Spann, G. R. Gladstone, D. V. Bisikalo, and V. I. Shematovich (2003), Summary of quantitative interpretation of IMAGE far ultraviolet auroral data, *Space Sci. Rev.*, *109*, 255–283, doi:10.1023/B:SPAC.0000007521.39348.a5.

Fuselier, S. A., S. P. Gary, M. F. Thomsen, E. S. Claflin, B. Hubert, B. R. Sandel, and T. Immel (2004), Generation of transient dayside subauroral proton precipitation, *J. Geophys. Res.*, *109*, A12227, doi:10.1029/2004JA010393.

Fuselier, S. A., S. M. Petrinec, K. J. Trattner, M. Fujimoto, and H. Hasegawa (2007), Simultaneous observations of fluctuating cusp aurora and low-latitude magnetopause reconnection, *J. Geophys. Res.*, *112*, A11207, doi:10.1029/2007JA012252.

Galand, M., and S. Chakrabarti (2006), Proton aurora observed from the ground, *J. Atmos. Ter. Phys.*, *68*, 1488–1501.

Galand, M., and D. Lummerzheim (2004), Contribution of proton precipitation to space-based auroral FUV observations, *J. Geophys. Res.*, *109*, A03307, doi:10.1029/2003JA010321.

Galand, M., J. Lilenstein, W. Kofman, and R. B. Sidje (1997), Proton transport model in the ionosphere: 1. Multistream approach of the transport equations, *J. Geophys. Res.*, *102*, 22,261–22,272.

Galand, M., R. Roble, and D. Lummerzheim (1999), Ionization by energetic protons in Thermosphere-Ionosphere Electrodynamics General Circulation Model, *J. Geophys. Res.*, *104*, 27,973–27,989.

Galand, M., T. J. Fuller-Rowell, and M. V. Codrescu (2001), Response of the upper atmosphere to auroral protons, *J. Geophys. Res.*, *106*, 127–139.

Galand, M., D. Lummerzheim, A. W. Stephan, B. C. Bush, and S. Chakrabarti (2002), Electron and proton aurora observed spectroscopically in the far ultraviolet, *J. Geophys. Res.*, *107*(A7), 1129, doi:10.1029/2001JA000235.

Galand, M., J. Baumgardner, D. Pallamraju, S. Chakrabarti, U. P. Lovhaug, D. Lummerzheim, B. S. Lanchester, and M. H. Rees (2004), Spectral imaging of proton aurora and twilight at Tromso, Norway, *J. Geophys. Res.*, *109*, A07305, doi:10.1029/2003JA010033.

Gattinger, R. L., A. Vallance Jones, J. H. Hecht, D. J. Strickland, and J. Kelly (1991), Comparison of ground-based optical observations of N2 second positive to $N2^+$ first negative emission ratios with electron precipitation energies inferred from the Sondre Stromfjord radar, *J. Geophys. Res.*, *96*, 11,341–11,351, doi:10.1029/91JA01015.

Hardy, D. A., L. K. Schmitt, M. S. Gussenhoven, F. J. Marshall, H. C. Yeh, T. L. Schumaker, A. Hube, and J. Pantazis (1984), Precipitating electron and ion detectors (S SJ/4) for the block 5D/flights 6-10 DMSP satellites: Calibration and data presentation, *Rep. AFGL-TR-Sd-0317*, Air Force Geophys. Lab., Hanscom Air Force Base, Mass.

Hardy, D. A., M. S. Gussenhoven, and D. Brautigam (1989), A statistical model of auroral ion precipitation, *J. Geophys. Res.*, *94*, 370–392.

Ivchenko, N., M. H. Rees, B. S. Lanchester, D. Lummerzheim, M. Galand, K. Throp, and I. Furniss (2004a), Observation of O^+ (^4P-$^4D^0$) lines in electron aurora over Svalbard, *Ann. Geophys.*, *22*, 2805–2817.

Ivchenko, N., M. Galand, B. S. Lanchester, M. H. Rees, D. Lummerzheim, I. Furniss, and J. Fordham (2004b), Observation of O^+ (^4P-$^4D^0$) lines in proton aurora over Svalbard, *Geophys. Res. Lett.*, *31*, L10807, doi:10.1029/2003GL019313.

Lanchester, B. S., M. H. Rees, K. J. F. Sedgemore, J. R. Palmer, H. U. Frey, and K. U. Kaila (1998), Ionospheric response to variable electric fields in small-scale auroral structures, *Ann. Geophys.*, *16*, 1343–1354.

Lanchester, B. S., D. Lummerzheim, A. Otto, M. H. Rees, K. J. F. Sedgemore-Schulthess, H. Zhu, and I. W. McCrea (2001), Ohmic heating as evidence for strong field-aligned currents in filamentary aurora, *J. Geophys. Res.*, *106*, 1785–1794.

Lanchester, B. S., M. H. Rees, S.C. Robertson, M. Galand, D. Lummerzheim, J. Baumgardner, M. Mendillo, I. Furniss, and A. D. Aylward (2003a), Proton and electron precipitation over Svalbard—First results from a new imaging spectrograph (HiTIES), in *Proceedings of the 28th Annual European Meeting of Atmospheric Studies by Optical Methods, SGO Publ. 92*, pp. 33–36, Sodankylä Geophys. Obs., Sodankylä, Finland.

Lanchester, B. S., M. Galand, S. C. Robertson, M. H. Rees, D. Lummerzheim, I. Furniss, L. M. Peticolas, H. U. Frey, J. Baumgardner, and M. Mendillo (2003b), High resolution measurements and modelling of auroral hydrogen emission line profiles, *Ann. Geophys.*, *21*, 1629–1643.

Lockwood, M., I. W. McCrea, G. H. Millward, R. J. Moffett, and H. Rishbeth (1993), EISCAT observations of ion composition and temperature anisotropy in the high-latitude *F*-region, *J. Atmos. Terr. Phys.*, *55*, 895–906.

Lockwood, M., B. S. Lanchester, H. Frey, K. Throp, S. Morley, S. E. Milan, and M. Lester (2003), IMF control of cusp proton emission intensity and dayside convection: Implications for component and anti-parallel reconnection, *Ann. Geophys.*, *21*, 955–982.

Lorentzen, D. A. (2000), Latitudinal and longitudinal dispersion of energetic auroral protons, *J. Geophys. Res.*, *105*, 12,733–12,745, doi:10.1029/1999JA900405.

Lorentzen, D. A., and J. Moen (2000), Auroral proton and electron signatures in the dayside aurora, *J. Geophys. Res.*, *105*, 12,733–12,745.

Lummerzheim, D., and J. Lilensten (1994), Electron transport and energy degradation in the ionosphere: Evaluation of the numerical solution, comparison with laboratory experiments and auroral observations, *Ann. Geophys.*, *12*, 1039–1051.

Lummerzheim, D., M. H. Rees, and G. J. Romick (1990), The application of spectroscopic studies of the aurora to thermospheric neutral composition, *Planet. Space Sci.*, *38*, 67–78.

Lummerzheim, D., M. Galand, J. Semeter, M. J. Mendillo, M. H. Rees, and F. J. Rich (2001), Emission of OI(630 nm) in proton aurora, *J. Geophys. Res.*, *106*, 141–148.

McCrea, I. W., M. Lester, T. R. Robinson, J. P. St.-Maurice, N. M. Wade, and T. B. Jones (1993), Derivation of the ion temperature partition coefficient β from the study of ion frictional heating events, *J. Geophys. Res.*, *98*, 15,701–15,715.

McWhirter, I., I. Furniss, A. D. Aylward, B. S. Lanchester, M. H. Rees, S. C. Robertson, J. Baumgardner, and M. Mendillo (2003), A new spectrograph platform for auroral studies in Svalbard, in *Proceedings of 28th Annual European Meeting of Atmospheric Studies by Optical Methods, 2SGO Publ. 92*, pp. 73–76, Sodankylä Geophys. Obs., Sodankylä, Finland.

Mende, S. B., et al. (2000), Far ultraviolet imaging from the IMAGE spacecraft, 3. Spectral imaging of Lyman-alpha and OI 135.6 nm, *Space Sci. Rev.*, *91*, 287–318.

Meurant, M., J.-C. Gérard, C. Blockx, B. Hubert, and V. Coumans (2004), Propagation of electron and proton shock-induced aurora and the role of the interplanetary magnetic field and solar wind, *J. Geophys. Res.*, *109*, A10210, doi:10.1029/2004JA010453.

Newell, P. T., and C.-I. Meng (1992), Mapping the dayside ionosphere to the magnetosphere according to particle precipitation characteristics, *Geophys. Res. Lett.*, *19*, 609–612, doi:10.1029/92GL00404.

Palmer, J. R. (1995), Plasma density variations in the aurora, Ph.D. thesis, Univ. of Southampton, Southampton, U. K.

Rees, M. H. (1982), On the interaction of auroral protons with the Earth's atmosphere, *Planet. Space Sci.*, *30*, 463–472.

Sigernes, F. (1996), Estimation of initial auroral proton energy fluxes from Doppler profiles, *J. Atmos. Terr. Phys.*, *58*, 1871–1883.

Simon, C., J. Lilensten, J. Moen, J. M. Holmes, Y. Ogawa, K. Oksavik, and W. F. Denig (2007), TRANS4: A new coupled electron/proton transport code—Comparison to observations above Svalbard using ESR, DMSP and optical measurements, *Ann. Geophys.*, *25*, 661–673.

Strickland, D. J., R. E. Daniell Jr., J. R. Jasperse, and B. Basu (1993), Transport-theoretic model for the electron-proton-hydrogen atom aurora: 2. Model results, *J. Geophys. Res.*, *98*, 21,533–21,548.

Vontrat-Reberac, A., D. Fontaine, P.-L. Blelly, and M. Galand (2001), Theoretical predictions of the effect of cusp and dayside precipitation on the polar ionosphere, *J. Geophys. Res.*, *106*, 28,857–28,865.

J. Baumgardner and S. Chakrabarti, Center for Space Physics, Boston University, Boston, MA 02215, USA.

M. Galand, Department of Physics, Imperial College London, London SW7 2AZ, UK.

N. Ivchenko, Space and Plasma Physics, School of Electrical Engineering, KTH, SE-100 44 Stockholm, Sweden.

O.-P. Jokiaho and B. S. Lanchester, School of Physics and Astronomy, University of Southampton, Southampton SO17 1BJ, UK. (b.s.lanchester@soton.ac.uk)

D. Lummerzheim, Geophysical Institute, University of Alaska Fairbanks, Fairbanks, AK 99775, USA.